PAPER

Free-anchored Nb_2O_5@graphene networks for ultrafast-stable lithium storage

To cite this article: Qinglin Deng *et al* 2018 *Nanotechnology* **29** 185401

IOP Publishing Nanotechnology
Nanotechnology 29 (2018) 185401 (11pp) https://doi.org/10.1088/1361-6528/aab083

Free-anchored Nb_2O_5@graphene networks for ultrafast-stable lithium storage

Qinglin Deng, Mengjiao Li, Junyong Wang, Kai Jiang[1], Zhigao Hu[1] and Junhao Chu

Key Laboratory of Polar Materials and Devices (MOE) and Technical Center for Multifunctional Magneto-Optical Spectroscopy (Shanghai), Department of Electronic Engineering, East China Normal University, Shanghai 200241, People's Republic of China

E-mail: kjiang@ee.ecnu.edu.cn and zghu@ee.ecnu.edu.cn

Received 2 January 2018, revised 6 February 2018
Accepted for publication 19 February 2018
Published 8 March 2018

Abstract

Orthorhombic Nb_2O_5 (T-Nb_2O_5) has structural merit but poor electrical conductivity, limiting their applications in energy storage. Although graphene is frequently adopted to effectively improve its electrochemical properties, the ordinary modified methods cannot meet the growing demands for high-performance. Here, we demonstrate that different graphene modified routes play a vital role in affecting the electrochemical performances of T-Nb_2O_5. By only manual shaking within one minute, Nb_2O_5 nano-particles can be rapidly adsorbed onto graphene, then the free-anchored T-Nb_2O_5@graphene three-dimensional networks can be successfully prepared based on hydrogel method. As for the application in lithium-ion batteries, it performs outstanding rate character (129 mA h g^{-1} (25C rate), 110 mA h g^{-1} (50C rate) and 90 mA h g^{-1} (100C rate), correspond to 79%, 67% and 55% capacity of 0.5C rate, respectively) and excellent long-term cycling feature (~70% capacity retention after 20000 cycles). Moreover, it still maintains similar ultrafast-stable lithium storage performances when Cu foil is substituted by Al foil as current collector. In addition, relevant kinetics mechanisms are also expounded. This work provides a versatile strategy for the preparation of graphene modified Nb_2O_5 or other types of nanoparticles.

Supplementary material for this article is available online

Keywords: Nb_2O_5@graphene, lithium-ion batteries, ultrafast-stable performances

(Some figures may appear in colour only in the online journal)

1. Introduction

Up to now, the most widely used energy storage systems for laptops, mobile phones and microelectronic devices have been the lithium-ion batteries (LIBs), owing to their obvious advantages, such as high energy density and superior stability [1–6]. However, the current commercial LIBs cannot meet the growing demand for preferable LIBs with higher capacity, faster charge-discharge rate, longer lifespan, as well as improved safety [7, 8]. As we know, graphite was frequently adopted as anode for LIBs, which has excellent electrical conductivity but a dissatisfied rate performance [9, 10]. Although some new anode materials with much higher capacity have been extensively studied, such as MoS_2 and SnS_2, the inferior capacity retention and poor charge–discharge rate restrict their applications [11–13]. Moreover, most of them have a low operating discharge voltage (below 1.0 V versus Li^+/Li), which would bring some underlying problems such as solid electrolyte interface (SEI) layer and lithium dendrite [14, 15]. Therefore, developing alternative anodes with high operating voltage (above 1.0 V versus Li^+/Li), excellent rate character and long cycling life, was raising more attention.

Recently, transition metal based electrode materials, such as MnO, Nb_2O_5, etc [1, 6, 16, 17]. Show charming energy storage performances. Among them, orthorhombic phase

[1] Authors to whom any correspondence should be addressed.

Nb_2O_5 (T-Nb_2O_5) is worthy of notice due to its higher discharge cut-off voltage and fast Li-ions insertion–extraction mechanism [14, 18–21]. It has a higher theoretical capacity (~200 mA h g^{-1}) than other familiar electrodes ($Li_4Ti_5O_{12}$ and TiO_2, ~170 mA h g^{-1}) [18, 22–25]. The insertion of lithium into Nb_2O_5 was not limited by the Li-ions solid-state diffusion, along with inapparent phase changes and low volume expansion [22, 26–29]. It is reported that the high-rate capability of T-Nb_2O_5 is attributed to its crystal structure, as most empty octahedral sites between (001) planes can provide natural tunnels for Li-ions transport [14, 30, 31]. However, its poor electrical conductivity (about 3.4×10^{-6} at 300 K) hinders its fast lithium storage kinetics [32–34]. One effective method is based on compositing T-Nb_2O_5 with conductive materials such as graphene and carbon nanotubes. Although there are some reports on carbon modified Nb_2O_5, the capacities and rate performances are urgently desired to improve for future applications [35–40]. More amount of carbon introduced into Nb_2O_5 can lead to better electrical conductivity, but bring the loss in capacity. Moreover, most of modification processes for Nb_2O_5@carbon are very complicated, limiting their commercial prospects [19, 30, 40]. Graphene was frequently adopted to effectively improve the electrical conductivity of Nb_2O_5, however, the ordinary modified routes, such as one-step hydrothermal method, cannot meet the growing demands for high electrochemical performances. Therefore, it is significant to propose an approach for obtaining the best performance with the minimum amount of graphene by a novel and feasible method.

In addition, the study and development of novel and high-efficiency electrode materials for supercapacitors has great significance. For example, Huang *et al* have done a lot of excellent research work on transition metal based electrode materials, such as MoS_2, $Li_4Ti_5O_{12}$, WO_3 and V_2O_5, which show excellent energy storage performances [5, 41–43]. As a very promising transition metal oxide, T-Nb_2O_5 could be as an ideal candidate to develop the Li-ions capacitors for the potential applications in electric vehicles and hybrid electric vehicle due to its fast pseudocapacitive kinetics [33, 35, 44–46]. Recently, nonaqueous hybrid supercapacitors (HSCs) has been a hot research topic. The insertion-type materials, such as TiO_2, $Li_4Ti_5O_{12}$, $TiNb_2O_7$ and Nb_2O_5, could be as the anode part of HSCs [47–51]. Owing to the unique properties of T-Nb_2O_5, it was believed that graphene modified T-Nb_2O_5 can further improve the performances of HSCs devices. Note that the prerequisite to achieve the above demand is to obtain a good T-Nb_2O_5@graphene electrode.

In the work, much efforts have been devoted to explore the methodologies for preparing T-Nb_2O_5@graphene composites, including one-step and two-steps hydrothermal reactions, and modified graphene hydrogel method. The T-Nb_2O_5@graphene derived from different synthetic routes show the discrepant electrochemical performances. We demonstrate that the free-anchored Nb_2O_5@graphene three-dimensional (3D) networks can be prepared by a versatile method based graphene hydrogel. It performs superior rate and cycling performances using the copper and aluminum foil as the anode current collector (capacity retention is over 70% after 20 000 cycles at 50C rate). In addition, relevant kinetics mechanisms and the application of HSCs device have been also investigated. It is believed that the present work could be helpful in proposing a novel strategy for the preparation of graphene modified Nb_2O_5 or other types of nanoparticles, accompanied with excellent energy storage performances.

2. Experimental section

2.1. Preparation of pristine Nb_2O_5, NG-1s, NG-2s and NG-3D

All of the chemical reagents and solvents used in the experiments were purchased from commercial sources and without any further purification. Graphene oxide (GO) was synthesized from natural graphite by a modified Hummers method. In a typical synthesis, 0.5 g of $NbCl_5$ (99.99%) was dissolved in 10 ml absolute ethyl alcohol (99.8%), named as Solution A. For pristine Nb_2O_5, Solution A was added into 60 ml deionized (DI) water, the mixture was stirred for 2 h, then transferred into a 100 ml polytetrafluoroethylene-lined stainless autoclave and hydrothermally treated at 180 °C for 15 h, followed by natural cooling to room temperature. The generated white precipitate was collected, named as Product B. In this work, three different synthesis routes were designed to prepare the Nb_2O_5@graphene composites. For one-step hydrothermal reaction (abbreviated as NG-1s), Solution A was added into 35 ml DI water and 25 ml GO aqueous solution (2 mg ml^{-1}), the mixture was stirred for 2 h, then transferred into a 100 ml polytetrafluoroethylene-lined stainless autoclave and hydrothermally treated at 180 °C for 15 h, followed by natural cooling to room temperature. For two-steps hydrothermal reaction (abbreviated as NG-2s), Product B was added into 25 ml DI water by ultrasonic dispersion, then 25 ml GO aqueous solution (2 mg ml^{-1}) was added into the mixture. It was stirred violently for 2 h to ensure homogeneous suspension, then transferred into a 100 ml polytetrafluoroethylene-lined stainless autoclave and hydrothermally treated at 180 °C for 15 h, followed by natural cooling to room temperature. For Nb_2O_5@graphene 3D networks (abbreviated as NG-3D), Product B was added into 20 ml DI water and a small quantity of HCl by ultrasonic dispersion, then excess sodium ascorbate dissolved in 8 ml DI water and 12.5 ml GO aqueous solution (2 mg ml^{-1}) were added into half of the mixture. It was mixed by only manual shaking within one minute. Finally, the suspension was transferred into a centrifuge tube and heated to 90 °C for 5 h. After cooling down to room temperature, the NG-3D hydrogel was obtained, and followed by immersion in DI water several times for removing the impurity ions, the obtained composite was further freeze-dried. Note that the as-prepared products except for NG-3D, were obtained by centrifugation, washed several times with DI water and absolute ethanol, and dried at 80 °C in vacuum for 20 h. The final Nb_2O_5@graphene composites were heated to 700 °C for 3 h under argon atmosphere.

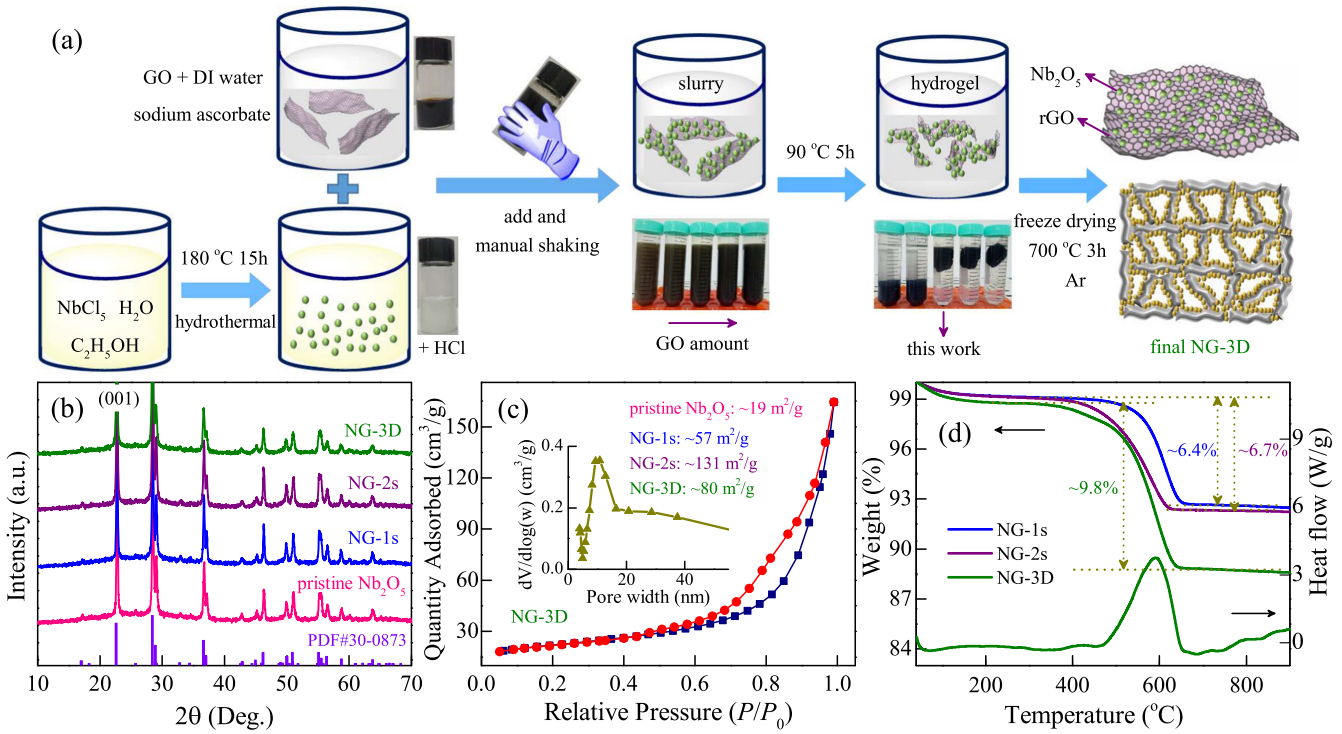

Figure 1. (a) Schematic illustration of the synthesis process for NG-3D. (b) XRD patterns of pristine Nb_2O_5, NG-1s, NG-2s and NG-3D. (c) Nitrogen adsorption–desorption isotherm and pore-size distribution (inset) for NG-3D. (d) Thermogravimetric analyses of NG-1s, NG-2s and NG-3D.

2.2. Characterization methods

The crystal structures were analyzed by x-ray diffraction (XRD, Cu Kα, D8 Advance, Bruker). Raman scattering experiments were carried out by a micro-Raman spectrometer (Jobin-Yvon LabRAM HR 800UV) with a 532 nm laser. In order to get rid of the trivial temperature dependence, all Raman spectra have been divided by the Bose–Einstein occupation number $n(\omega) + 1 = 1/[1 - \exp(-\hbar\omega/k_BT)]$. The Brunauer–Emmett–Teller (BET) surface areas of the powder samples were measured by a surface area analyzer (TriStar II 3020) using N_2 at 77 K, and the pore-size distribution curves were obtained using Barrett–Joiner–Halenda model. Thermogravimetric analyses (TGA) and differential scanning calorimetry (DSC) of samples were performed in a TGA/DSC 1 STAR^e System (Mettler-Toledo) from 40 °C to 900 °C with a heating rate of 15 °C min^{-1}. X-ray photoelectron spectroscopy (XPS) measurements were carried out on a Thermo ESCALAB 250XI system with Al-Kα radiation ($h\nu = 1486.6$ eV). The surface morphologies of powder samples were examined by field emission scanning electron microscopy (SEM, FEI Quanta 400 FEG). The transmission electron microscopy (TEM) images and selected area electron diffraction (SAED) of the as-synthesized composites were acquired by TEM (FEI Tecnai G2 F20) with an acceleration voltage of 200 kV, equipped with an energy dispersive x-ray spectroscopy (EDX) detector for elemental mapping.

2.3. Electrochemical tests

Two-electrode coin-cell assembled in an argon-filled glovebox, was adopted to investigate the energy storage applications. For half-cell test of the LIBs, the synthesized samples were used as the working electrode, which were fabricated by casting a slurry of 80 wt% active material, 10 wt% acetylene black, and 10 wt% polyvinylidene fluoride in N-methyl-2-pyrrolidinone on a copper/aluminum foil, then dried at 90 °C in vacuum for 24 h. The active material mass loading was ~1.0–3.0 mg cm^{-2}. The lithium foil was used as counter and reference electrodes, a membrane (Celgard 2400) as the separator, and the electrolytes were 1 mol l^{-1} $LiPF_6$ solution in a 1:1:1 (by volume) mixture of ethylene carbonate, dimethyl carbonate and ethyl methyl carbonate. The commercial activated carbon (AC) electrode was prepared following the same method as mentioned above, but only using aluminum foil as the current collector. For full-cell tests of the HSCs, the electrodes of synthesized samples (based on copper foil) were used as the anode and the AC electrodes as the cathode, in the potential range of 0.5–3.0 V. The assembled steps were the same as mentioned above. Galvanostatic charge–discharge experiments were performed using battery measurement system (LAND-CT2001A) and an electrochemical workstation (CHI660E). Cyclic voltammetry (CV) curves at a sweep rate of 0.1–10.0 mV s^{-1}, and electrochemical impedance spectroscopy (EIS) with an amplitude of 5 mV in the frequency range 100 kHz–0.1 Hz, were tested on an

electrochemical workstation (CHI660E). All electrochemical measurements were carried out at room temperature.

3. Results and discussion

3.1. Synthesis mechanisms, XRD, Raman, BET, TGA and XPS analysis

Figures 1(a) and S1 is available online at stacks.iop.org/NANO/29/185401/mmedia schematically illustrates the typical synthetic procedures for pristine Nb_2O_5, NG-1s, NG-2s and NG-3D. As a typical example, for NG-3D, the generated amorphous niobium oxide nanoparticles can be freely and uniformly anchored onto the GO surface due to the electrostatic attraction under acidic condition. Then, the sodium ascorbate was added into the mixture for the reduction of GO into reduced GO (rGO) under the thermal treatment. Finally, a hybrid hydrogel of Nb_2O_5@graphene was formed. Owing to the unique features and porosity of NG-3D, it was believed that such system could bring multi-dimensional electron transport pathways for LIBs.

Figure 1(b) shows the XRD patterns of as-prepared powder samples. As we can see, all of them display similar diffraction peaks and match with the orthorhombic phase of Nb_2O_5 (T-Nb_2O_5, JCPDS No. 30-0873). Raman scattering spectra of pristine Nb_2O_5, NG-1s, NG-2s and NG-3D were shown in figure S2. It was found that all samples show a strong phonon band around 680 cm^{-1}, which belongs to the Nb–O–Nb bridging bond [8, 33]. The NG-1s, NG-2s and NG-3D nanocomposites show distinctive D (disordered carbon) and G (graphitic carbon) scattering bands at around 1340 and 1580 cm^{-1}, respectively.

The porous structure and specific surface area of all samples are investigated using N_2 adsorption–desorption isotherms at 77 K. As shown in figures S3 and 1(c), the BET specific surface areas of pristine Nb_2O_5, NG-1s, NG-2s and NG-3D are about 19, 57, 131 and 80 $m^2\ g^{-1}$, respectively. As a typical example, NG-3D exhibits a characteristic isotherm of type IV. The adsorbed volume gradually increases with an evident hysteresis loop ($0.4 < P/P_0 < 1$), suggesting the existence of a mesoporous structure. The pore diameter of NG-3D is located at about 4 nm, 10 nm and over 20 nm with a broad pore size distribution, as shown in the inset of figure 1(c). The satisfactory specific surface area could be attributed to the introduction of graphene 3D aerogel. Such 3D networks could maximize the contact with the electrolyte for LIBs and HSCs, and it was expected to exhibit excellent electrical performances. Moreover, as shown in figure 1(d), the weight percentage of graphene in NG-1s, NG-2s and NG-3D nanocomposites based on TGA-DSC analysis were estimated to be ~6.4, 6.7 and 9.8 wt%, respectively.

Figure S4 shows the XPS spectrum of pristine Nb_2O_5, NG-1s, NG-2s and NG-3D. As we can see, C, Nb and O elements can be detected on the surface. The Nb 3d XPS spectra of pristine Nb_2O_5 were observed at 210.08 eV and 207.34 eV for the $3d_{3/2}$ and $3d_{5/2}$ peaks, respectively, and the distance between the two peaks is about 2.74 eV, which is in good agreement with the findings in the core level spectra of Nb_2O_5 [29, 52]. After combining with graphene, the binding energy of $3d_{3/2}$ and $3d_{5/2}$ peaks shift toward a higher energy.

3.2. Surface morphologies

The morphology and structure of as-synthesized samples are characterized by SEM and TEM. As shown in figure S5, the hydrothermal derived pristine Nb_2O_5 has nanoparticle patterns with the homogeneous size, and they inevitably agglomerate to form clusters. For NG-1s and NG-2s, after combining with Nb_2O_5 nanoparticles, the surface of graphene became rough. Interestingly, owing to the advantages of two-steps hydrothermal reaction, most of synthesized Nb_2O_5 nanoparticles can be well-dispersed on the surface of graphene sheets (shown in figure 2(c)). However, for NG-1s, figure 2(b) indicates that some Nb_2O_5 nanoparticles solely agglomerate without combining with graphene. As shown in figure 2(a), NG-3D has a cross-linked 3D porous structure like pure graphene aerogel, while the graphene sheets are uniformly decorated with Nb_2O_5 nanoparticles. The 3D graphene networks play a key role in hindering the aggregation of Nb_2O_5 nanoparticles. The TEM images of NG-3D were shown in figures 2(d) and (e), the corresponding SAED image is also provided. Obviously, the distributed Nb_2O_5 nanoparticles are tightly anchored onto the surface of graphene sheets. The average particle size was estimated to about 25 nm. In addition, some vital information about the crystal structure of NG-3D can be obtained from the high-resolution TEM images. It was found that NG-3D exhibits high crystallinity with a spacing of 0.39 nm of the lattice fringes, which corresponds to the (001) plane of T-Nb_2O_5, as shown in the inset of figure 2(e). From the EDX mapping analysis (shown in figure 2(f)), it further verifies the uniform distribution of Nb, O and C elements. Expectedly, the different synthetic routes lead to the discrepant morphology. For instance, in comparison with the TEM images of NG-1s, NG-2s and NG-3D, obviously, NG-1s has the biggest grain size, while NG-3D has the smallest one. Due to the shortened diffusion length and conductive 3D carbon networks, NG-3D would possess huge advantages for energy storage applications.

3.3. Energy storage applications

The energy storage performances of as-prepared samples were investigated using two-electrode coin-cell. Figures S6 and 3(a) show the typical CV curves of pristine Nb_2O_5, NG-1s, NG-2s and NG-3D, in the potential window of 1.0–3.0 V (versus Li^+/Li) at a sweep rate of 0.5 mV s^{-1}. As an example, NG-3D exhibits broad cathodic and anodic peaks in the voltage range of 1.0–2.0 V, which is derived from the redox reaction of Nb ($Nb_2O_5 + xLi^+ + xe^- \Longleftrightarrow Li_xNb_2O_5$, x is the mole fraction of the inserted lithium ions) [26, 53, 54]. Detailedly, for NG-3D, the reduction peaks are observed at about 1.55 and 1.79 V versus Li^+/Li during the first reduction process (Li insertion), and the oxidation peaks are observed at about 1.83 and 1.98 V versus Li^+/Li during the first oxidation process (Li extraction). The subsequent curves show quite good reproducibility. In order to explore the kinetic

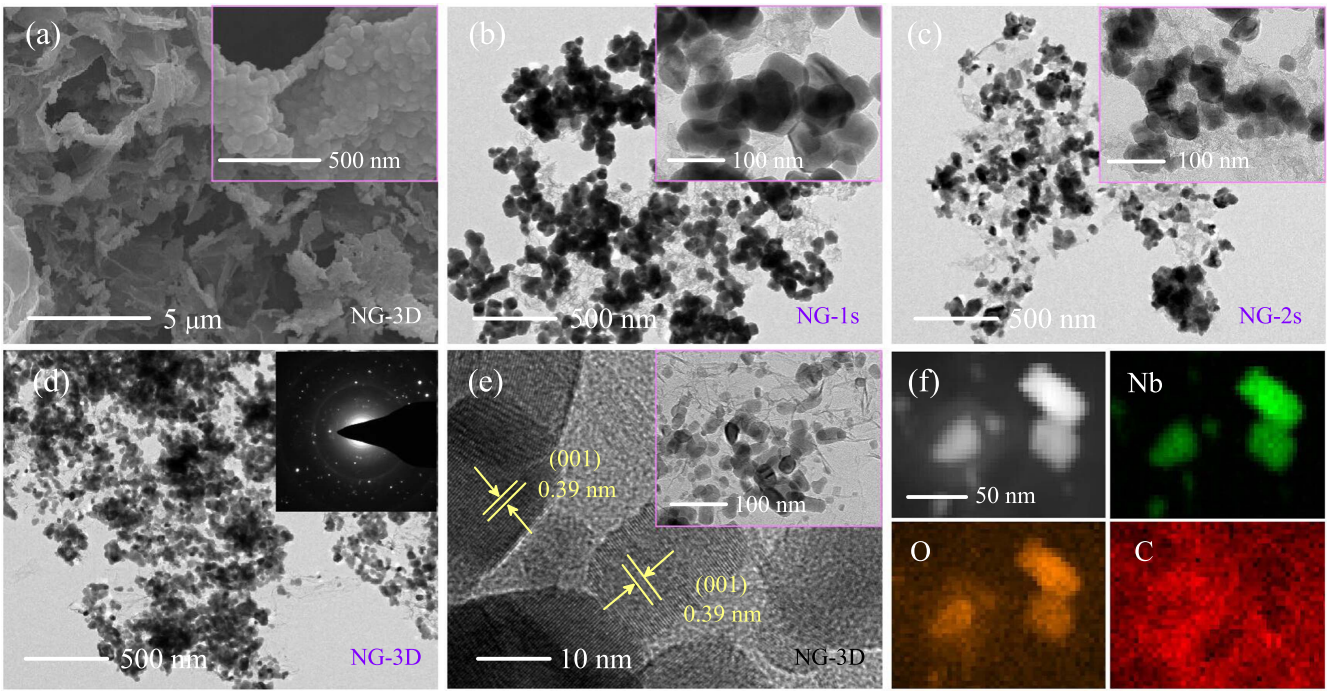

Figure 2. (a) SEM images of NG-3D under different magnifications. TEM images of (b) NG-1s, (c) NG-2s, and (d), (e) NG-3D under different magnifications. (f) TEM images of NG-3D with elemental mapping of Nb, O, and C.

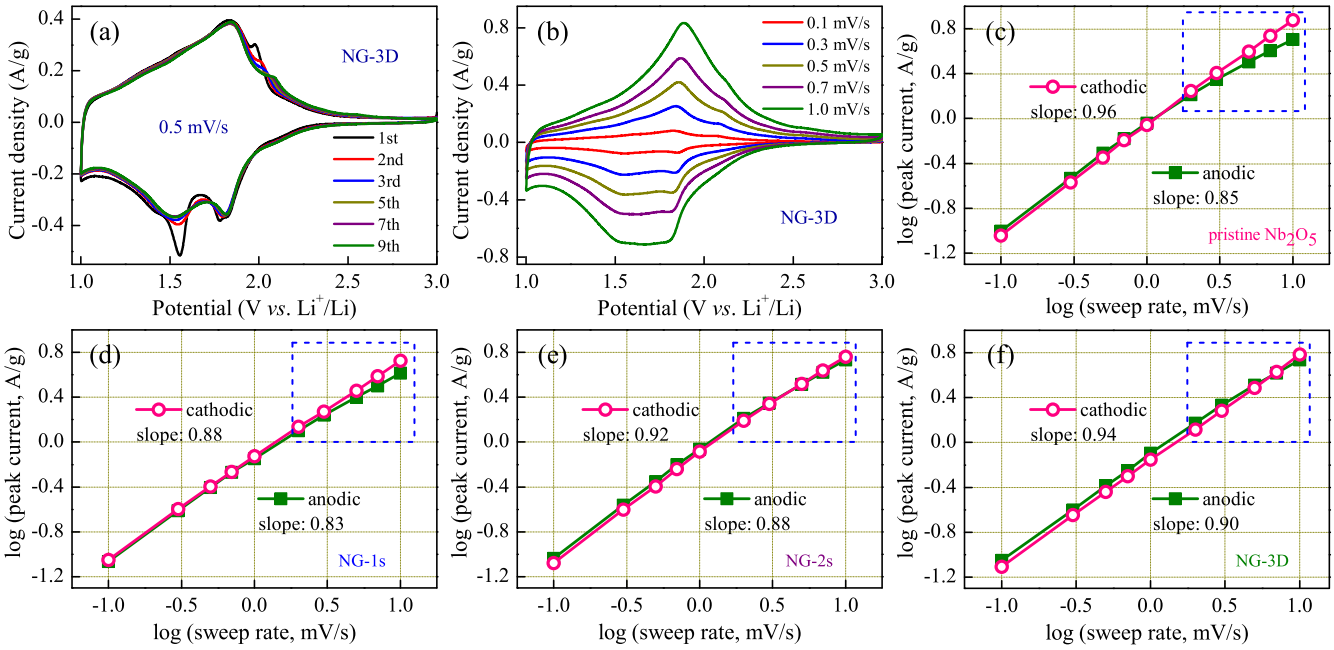

Figure 3. Electrochemical performances of pristine Nb_2O_5, NG-1s, NG-2s and NG-3D using the copper foil as the anode current collector. Note that the active material mass loading was ~1 mg cm^{-2}. Cyclic voltammetry (CV) curves of NG-3D measured (a) at a sweep rate of 0.5 mV s^{-1}, (b) at various sweep rates from 0.1 to 1 mV s^{-1} in the voltage range of 1.0–3.0 V (versus Li^+/Li). The corresponding specific peak currents characterized at different sweep rates for (c) pristine Nb_2O_5, (d) NG-1s, (e) NG-2s and (f) NG-3D. Note that the dashed box points out the obvious changes.

mechanisms of Li-ion insertion–extraction behaviors for pristine Nb_2O_5, NG-1s, NG-2s and NG-3D, the CV experiments with various sweep rates were carried out, as shown in figures S6 and 3(b). The CV curves follows the power law: [26, 30, 33] $i = av^b$, where a and b are adjustable parameters, i is the current, and v is the sweep rate. The value of b is close to 0.5 and 1, corresponds to the diffusion-limited contribution and surface-controlled pseudocapacitive reaction, respectively. Figures 3(c)–(f) show the specific peak current of pristine Nb_2O_5, NG-1s, NG-2s and NG-3D, respectively, at different sweep rates in range of 0.1–10.0 mV s^{-1}. Note that the current of reduction peak (at about 1.55 V) and oxidation

peak (at about 1.83 V) were chosen as the peak current. As can be seen, the *b* values based on anodic and cathodic peak currents for pristine Nb_2O_5, NG-1s, NG-2s and NG-3D are close to 1, which demonstrates that the kinetic of lithium storage for all samples is mainly derived from surface-controlled pseudocapacitive reaction. It was believed that such mechanism would provide a high-rate Li-ion insertion–extraction process. Among them, the *b* values of NG-3D were more close to 1, as compared with other samples. Moreover, the dashed box points out the obvious changes of anodic and cathodic curves. It was found that the specific cathodic peak current of pristine Nb_2O_5 exceed the anodic values when the sweep rate increases to 2 mV s^{-1}. The difference value between the cathodic and anodic peak current increases with increasing the sweep rate, indicating the poor reproducibility of cathodic and anodic process under high rate density. For NG-1s, it has the similar phenomenon with pristine Nb_2O_5, while the difference value between the cathodic and anodic peak current was smaller than pristine Nb_2O_5 at the same sweep rate. For NG-2s, the specific cathodic peak current were close to anodic values when the sweep rate is over 2 mV s^{-1}. For NG-3D, the specific cathodic peak current exceed the anodic value until the sweep rate increases to 10 mV s^{-1}. The cathodic and anodic curves of NG-3D maintain a good linear relationship below 5 mV s^{-1}. In comparison with the curves of pristine Nb_2O_5, NG-1s, NG-2s and NG-3D, they successively present the better reproducibility of cathodic and anodic process under high sweep rate, indicating that NG-3D might perform superior electrochemical performances.

As we know, rate performance is one of the most important characters for evaluating the LIBs. Figure 4(a) shows the evolution of the specific capacity for pristine Nb_2O_5, NG-1s, NG-2s and NG-3D at different current densities. Obviously, NG-3D presents the best rate performances. Figure S7 shows the electrochemical performances of rGO. As we can see, rGO has a low operating discharge voltage (below 1.0 V versus Li^+/Li), with a very low specific capacity in the potential window of 1.0–3.0 V (versus Li^+/Li). Thus, rGO shows negligible effect on the electrochemical performances of NG-3D in the potential window of 1.0–3.0 V (versus Li^+/Li). In detail, due to the absence of graphene, the pristine Nb_2O_5 has a highest specific capacity of about 183 mA h g^{-1} than others at the current density of 0.5C (equal to 100 mA g^{-1}). With increasing the current density, the specific capacities of all samples gradually decrease. With respect to pristine Nb_2O_5, as expected, it has relatively lower capacity under high rate due to poor electrical conductivity. Note that the pristine Nb_2O_5 electrode is inferior than others at the same coating process. NG-3D still possesses a high specific capacity of about 129 mA h g^{-1} (25C rate) and 110 mA h g^{-1} (50C rate), which correspond to 79% and 67% capacity retention, respectively, as compared with the 0.5C rate (about 163 mA h g^{-1}). After undergoing a high current density of 50C, the specific capacity of NG-3D can be maintained when the current density comes back again to 1C. Correspondingly, figure 4(b) presents the typical galvanostatic charge–discharge (GCD) profile of NG-3D electrode at different current densities in range of 0.5C–50C. Obviously, with increasing charge–discharge current densities, the specific capacity of NG-3D decreases gradually. Note that the rate performance of NG-3D presents a tremendous competitive advantage, as compared with the most previously reported results of pure and modified Nb_2O_5 [29, 30, 33, 35, 53, 55]. Moreover, the cycling performance was further evaluated at a current density of 2C (equal to 400 mA g^{-1}), as shown in figure 4(c). Due to the possible activation process, the specific capacity of NG-3D and NG-2s slightly increases in the first 50 cycles, then maintains a relatively stable value. However, for pristine Nb_2O_5, combining with the GCD profiles (shown in figure S8), it fades dramatically after 1000 cycles with a low capacity retention of about 36%. The capacity of NG-1s show a dramatic decrease after 200 cycles, then maintains a relatively stable value. Moreover, the EIS of these four samples after 1000th cycle (at a current density of 400 mA g^{-1}) are compared in figure 4(d). In the Nyquist plots, it is obvious that all of them have a similar contact resistance at high frequency. Except for pristine Nb_2O_5, others show lower charge transfer resistance at medium frequency with the similar semicircles. The straight line at low frequency represents the mass transfer of Li-ions. As we can see, NG-3D shows the low charge transfer resistance and fast Li-ions diffusion behavior. In addition, the cyclic stability of the activated NG-3D electrode at a higher rate of 50C has been demonstrated. As shown in figure 4(e), NG-3D shows ultrastable cycling performance of over 20 000 cycles with a high capacity retention of ~70%.

In addition, the effects of mass loading on electrochemical performances for NG-3D have been investigated, as shown in figure 4(f). Obviously, the mass loading can dramatically affect the rate performances. In detail, when the mass loading was 1–3 mg cm^{-2}, they have the similar electrochemical performances below 10C rate. As the current density increase to a higher value, they show the apparent differences. The reason can be attributed to the increasing ion diffusion limitations in thicker electrodes. Note that these electrodes were prepared using the same coating technique, which is hard to obtain a high-quality thicker electrode. However, NG-3D has the potential ability to realize the excellent rate performances at higher mass loading if ameliorate the coating process. As we know, good anode material should has the fast lithium insertion kinetics. For half-cell test of the LIBs, it is equal to the high discharge rate. In order to further investigate the energy storage applications of NG-3D, the rate experiments at various charge current densities from 25C to 1C, with a constant discharge rate of 25C were carried out, as shown in figures 4(g) and (h). As we can see, the time of lithium insertion is very short at 25C discharge rate, however, NG-3D can still maintain a stable specific capacity of about 130 mA h g^{-1} during different charge rate of 25C–1C. It indicates that NG-3D can be applied to high-rate LIBs which can fastly charge and slowly discharge.

It is noteworthy that NG-3D shows superior rate and cycling performance above 1.0 V versus Li^+/Li, which can avoid the formation of SEI films, lithium dendrite and Li–Al alloy. Therefore, copper foil can be substituted by cheaper and lighter aluminum foil as the anode current collector, and the relevant experiments have been carried out. The kinetic mechanisms of Li-ion insertion–extraction behavior for

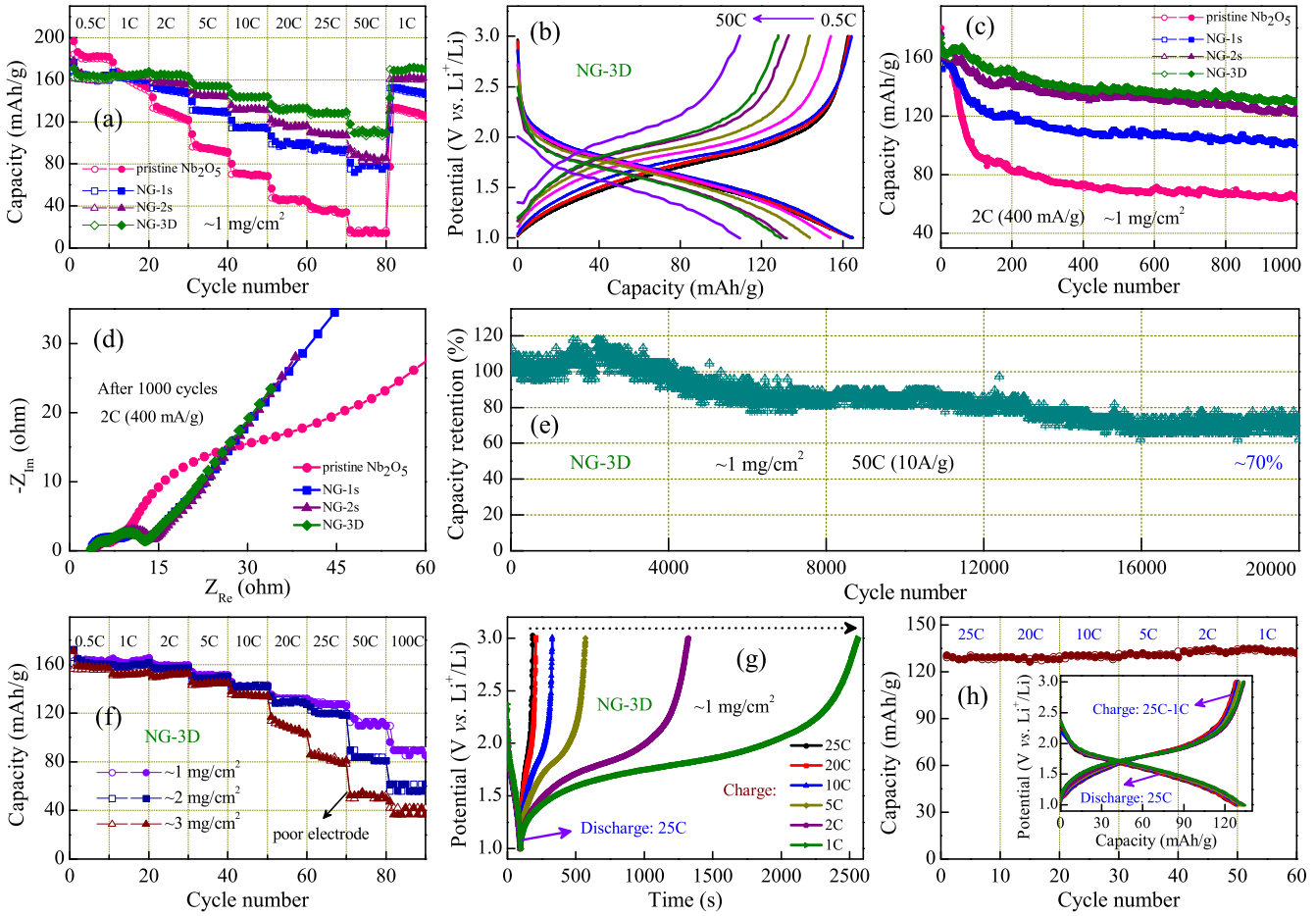

Figure 4. Electrochemical performances of pristine Nb_2O_5, NG-1s, NG-2s and NG-3D using the copper foil as the anode current collector. (a) Rate performance of pristine Nb_2O_5, NG-1s, NG-2s and NG-3D at different current densities. (b) Galvanostatic charge–discharge (GCD) profiles of NG-3D at different rates. (c) Cycling stability of pristine Nb_2O_5, NG-1s, NG-2s and NG-3D at a current density of 400 mA g^{-1} (2C rate). (d) Nyquist plots of pristine Nb_2O_5, NG-1s, NG-2s and NG-3D after 1000 cycles (2C rate), in the frequency range of 100 kHz–0.1 Hz. (e) Cycling stability of NG-3D at 50C rate. (f) Comparison of rate performance for NG-3D under different mass loadings (~1–3 mg cm^{-2}) in the current density range of 0.5C–100C. (g) GCD profiles and (h) rate performance for NG-3D at various charge current densities from 25C to 1C, with a constant discharge current density of 25C.

NG-3D together with using aluminum foil as the current collector, were firstly investigated. Figures 5(a) and S9 show the CV curves of NG-3D measured at various sweep rates from 0.1 to 1 mV s^{-1} and at a sweep rate of 0.5 mV s^{-1}, respectively, in the voltage range of 1.0–3.0 V (versus Li$^+$/Li). As shown in figure 5(b), it was found that the *b* values based on anodic and cathodic peak currents are close to 1, which is very similar to the results of using copper foil as the current collector. It reveals that the kinetic of lithium storage is also mainly controlled by the capacitive contribution. NG-3D electrode using aluminum foil as the current collector, was also expected to exhibit excellent lithium storage applications. Figure 5(c) shows the evolution of the specific capacity for pristine Nb_2O_5 and NG-3D, which use the aluminum foil as the current collector, at different current densities in range of 0.5C–50C. Unfortunately, pristine Nb_2O_5 shows the ultra-poor rate performance, as all of the basic capacity is lost when the rate increases to 5C (equal to 1 A g^{-1}). The main reasons could be due to the poor electrical conductivity of pristine Nb_2O_5 and the dissatisfied adhesivity between the active material and commercial aluminum foil. However, combining with the GCD profiles (shown in figure S10), NG-3D still has a high specific capacity of about 101 mA h g^{-1} at 25C rate, which corresponds to 62% capacity retention, as compared with the 0.5C rate (about 164 mA h g^{-1}). It is a pity that using aluminum foil as the current collector did not show the same capacity retention as copper foil. The reasons might be attributed to the poorer electrical conductivity and adhesivity of commercial aluminum foil than copper foil. In addition, the cycling performance of the activated NG-3D electrode was further evaluated at a current density of 50C, as shown in figure 5(d). It also shows ultra-stable cycling performance of over 20 000 cycles with a high capacity retention of ~75%. Moreover, figure 5(e) shows the rate experiments at various charge rate from 25C to 1C, with a constant 25C discharge rate. Combining with the GCD profiles (shown in figure S10), it was found that with decreasing the current density, the specific capacities of NG-3D gradually increase. It possesses a high capacity retention of ~92% after 2000 cycles. The above results demonstrate that cheaper and lighter aluminum foil can be used as the anode current collector of LIBs for NG-3D. In addition, table 1 shows the comparison on electrochemical

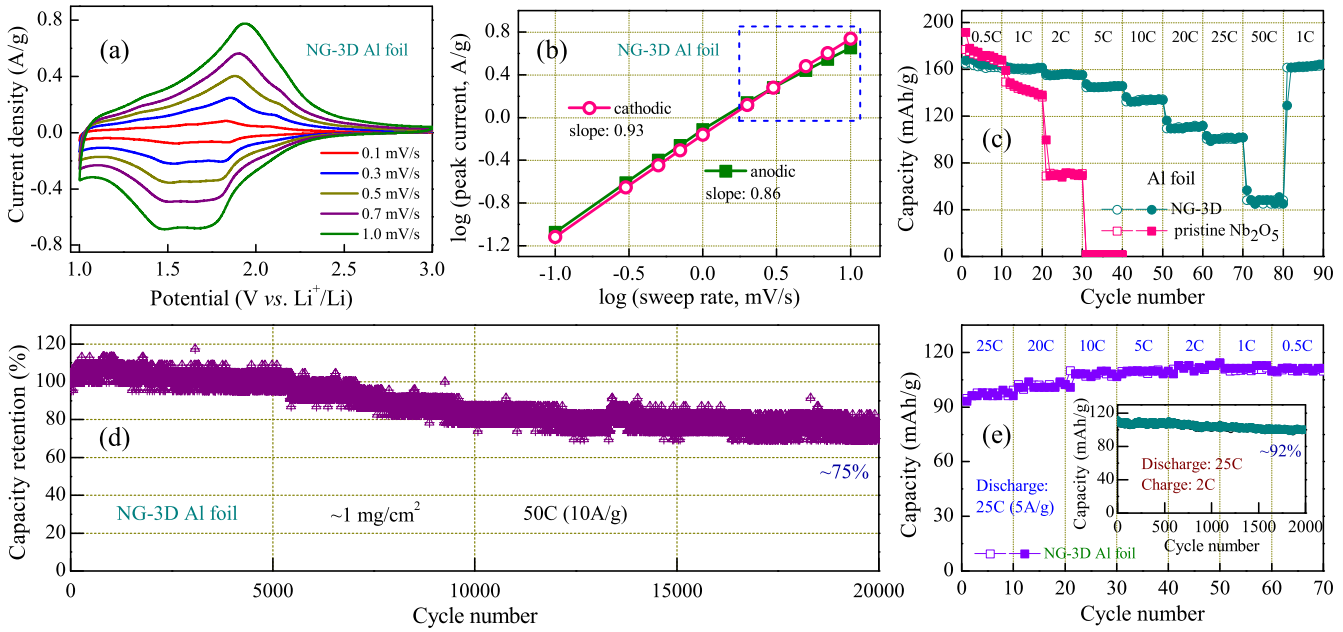

Figure 5. Electrochemical performances of pristine Nb_2O_5 and NG-3D using the aluminum foil as the anode current collector. Note that the active material mass loading was ~1 mg cm^{-2}. (a) Cyclic voltammetry (CV) curves of NG-3D measured at various sweep rates from 0.1 to 1 mV s^{-1} in the voltage range of 1.0–3.0 V (versus Li^+/Li). (b) The corresponding specific peak currents characterized at different sweep rates for NG-3D. Note that the dashed box points out the obvious changes. (c) Rate performance of pristine Nb_2O_5 and NG-3D at different current densities. (d) Cycling stability of NG-3D at 50C rate. (e) Rate performance for NG-3D at various charge current densities from 25C to 1C, with a constant discharge current density of 25C.

Table 1. Electrochemical performance (LIBs) comparison for NG-3D to the literature.

	Rate performance (capacity, mA h g^{-1})				Cycling stability			
Electrode architecture	Capacity (current)	1 A g^{-1}	5 A g^{-1}	10 A g^{-1}	Current	Cycle numbers	Retention	References
NG-3D (1 mg cm^{-2})	163 (0.1 A g^{-1})	154	129	110	10 A g^{-1}	20000	70%	This work
NG-3D (Al foil) (1)	164 (0.1)	155	101	48	10	20000	75%	This work
Nb_2O_5/HGF-2.0 (1)	191 (0.2)	162	—	107	—	—	—	[1]
Ag-N-Nb_2O_5 (1.5)	241 (0.05)	155	87	—	3	3000	69	[29]
T-Nb_2O_5@C NCs (0.9–1.1)	171 (0.1)	120	84	—	—	—	—	[30]
T-Nb_2O_5 QDs MOF (1)	198 (0.2)	143	105	—	1	1000	141	[33]
L-Nb_2O_5 NWs/rGO (–)	160 (0.2)	132	95	—	5	1000	93	[35]
urchin-like Nb_2O_5 (1.2–1.6)	175 (0.2)	135	90	—	1	1000	131	[53]
m-T-Nb_2O_5 NFs (1.5)	197 (0.1)	156	70	—	3	5000	88	[55]
TiO_2@CNS spheres (–)	198 (0.17 A g^{-1})	136 (1.68)	87 (3.35)	—	1.68	500	136	[56]
$Li_4Ti_5O_{12}$ micro-spheres (–)	175 (0.09 A g^{-1})	139 (1.75)	108 (5.25)	—	5.25	1000	102	[57]
3DOM $TiNb_2O_7$ (1)	206 (0.39 A g^{-1})	124 (1.94)	84 (7.74)	—	3.87	1000	87	[58]

performances of some Nb_2O_5-based anode materials and other similar materials, which are taken from the previous typical reports with the excellent performances in LIBs. Our work shows the excellent rate character and longer lifespan with a high capacity retention.

In order to better expound the fast lithium insertion–extraction kinetics, figures 6(a) and (b) show the TEM images of NG-3D (Cu foil) after 1000 cycles (2C rate) and after 20000 cycles (50C rate), respectively. It was found that the morphology was not destroyed and the grain size did not obviously changed after high-rate charge–discharge and long cycling tests. Figure 6(c) depicted the possible mechanisms of lithium ions insert/extract into NG-3D. Owing to the high BET surface area and conductive 3D carbon networks, which can effectively improve the electrical conductivity, relax the volume expansion and increase the contact area of the

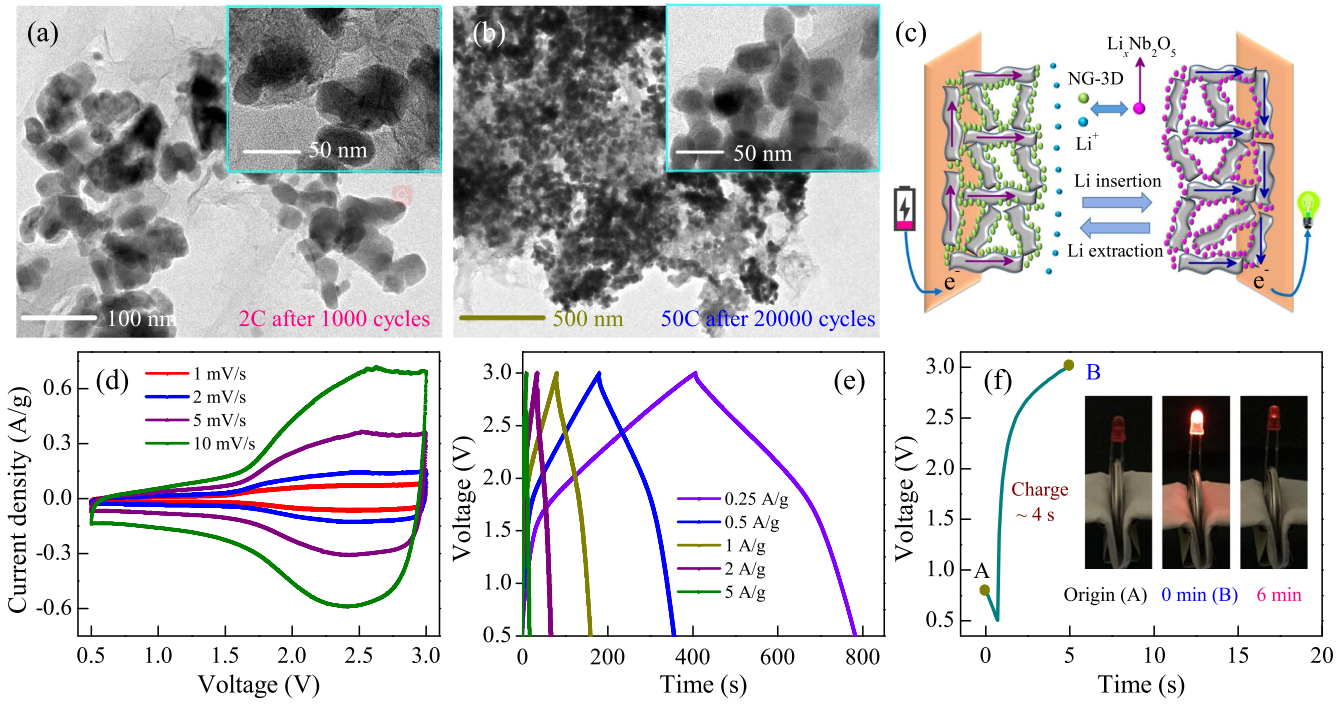

Figure 6. (a) The TEM images of NG-3D (Cu foil) (a) 2C after 1000 cycles and (b) 50C after 20 000 cycles. (c) The possible mechanisms of lithium ion insertion/extraction for NG-3D. (d) Cyclic voltammetry (CV) curves at various sweep rates from 1 to 10 mV s^{-1} for the HSCs devices using NG-3D nanocomposite and commercial activated carbon (AC) electrode as the anode and cathode, respectively. (e) Galvanostatic charge–discharge (GCD) profiles at various current densities from 0.25 to 5 A g^{-1}. (f) The photograph of a red LED powered by one HSCs device.

electrolyte, NG-3D shows superior lithium storage performances. The excellent rate character and cycling stability of NG-3D make it wide potential in Li-ion capacitors. In this work, non-aqueous HSCs were fabricated using NG-3D nanocomposite and commercial AC electrode as the anode and cathode, respectively. For HSCs, during the charging process, Li^+ fastly intercalate into the Nb_2O_5 crystal, while PF_6^- rapidly adsorb on the AC electrolyte surface, and discharging is the reverse process. Figure 6(d) shows the asymmetrical CV curves of the HSCs device at various sweep rates from 1 to 10 mV s^{-1} in the voltage range of 0.5–3.0 V. Moreover, the GCD profiles (shown in figure 6(e)) exhibit nontypical triangular shapes at various current densities from 0.25 to 5 A g^{-1}. Note that the current densities are based on the total weight of active anode and cathode. Figure 6(f) shows the practical applications of the NG-3D//AC HSCs device. It was found that using one coin cell, which charges to 3.0 V by only ~4 s, can still light up a red LED for more than 6 min. In addition, in order to better compare and illuminate the energy and power features of NG-3D//AC HSCs device and others in previous reports, Ragone plot is plotted in figure S11. As we can see, our assembled HSCs device can reach a high energy density and power density. The high energy density was not observed when drastically increase the current density. The reason might be attributed to the high voltage drop caused by various resistances in the device. Comparing with previous reports on the excellent performances of nonaqueous HSCs devices, such as T-Nb_2O_5 QDs MOF//AC [33], C-T-Nb_2O_5//AC [44], T-Nb_2O_5@C NCs//AC [30], m-Nb_2O_5-C//AC [46], in our work, the NG-3D//AC HSCs device shows the comparable energy density at the same power density.

4. Conclusion

In conclusion, we have systematically compared the effects of three different synthetic routes on electrochemical performances for T-Nb_2O_5@graphene composites. In particular, a versatile method based graphene hydrogel has been proposed to prepare the free-anchored T-Nb_2O_5@graphene 3D networks (NG-3D). Significantly, the NG-3D performs excellent rate feature. For instance, it still possesses a high specific capacity of about 129 mA h g^{-1} (25C rate) and 110 mA h g^{-1} (50C rate), which correspond to 79% and 67% capacity retention, respectively, as compared with the 0.5C rate (about 163 mA h g^{-1}). It also shows ultra-stable cycling performance of over 20 000 cycles with a high capacity retention of ~70%. Moreover, when the copper foil was substituted with cheaper and lighter aluminum foil as the anode current collector, it still has a high specific capacity of about 101 mA h g^{-1} at 25C rate. It also shows ultra-stable cycling performance of over 20 000 cycles with a high capacity retention of ~75%. Therefore, we conclude that the present work not only prepare the novel NG-3D composite, which shows ultrafast-stable lithium storage performances, but also can be helpful in applying this novel synthetic route for ameliorating the poor electrical conductivity of other similar nanoparticles.

Acknowledgments

This work was financially supported by Major State Basic Research Development Program of China (Grant Nos. 2013CB922300), Natural Science Foundation of China (Grant Nos. 61674057, 11374097, 61376129, 61504156, and 61227902), Projects of Science and Technology Commission of Shanghai Municipality (Grant Nos. 15JC1401600 and 14XD1401500), and the Program for Professor of Special Appointment (Eastern Scholar) at Shanghai Institutions of Higher Learning.

ORCID iDs

Zhigao Hu https://orcid.org/0000-0003-0575-2191

References

[1] Sun H T *et al* 2017 Three-dimensional holey-graphene/niobia composite architectures for ultrahigh-rate energy storage *Science* **356** 599–604
[2] Zhao Y, Li X, Yan B, Xiong D, Li D, Lawes S and Sun X 2016 Recent developments and understanding of novel mixed transition-metal oxides as anodes in lithium ion batteries *Adv. Energy Mater.* **6** 1502175
[3] Zhang K, Lee G-H, Park M, Li W and Kang Y-M 2016 Recent developments of the lithium metal anode for rechargeable non-aqueous batteries *Adv. Energy Mater.* **6** 1600811
[4] Tang Y, Zhang Y, Li W, Ma B and Chen X 2015 Rational material design for ultrafast rechargeable lithium-ion batteries *Chem. Soc. Rev.* **44** 5926–40
[5] Zhang W J and Huang K J 2017 A review of recent progress in molybdenum disulfide-based supercapacitors and batteries *Inorg. Chem. Front.* **4** 1602–20
[6] Zhang J, Zhang W, He T, Amiinu I S, Kou Z K, Li J N and Mu S C 2017 Smart reconstruction of dual-carbon decorated MnO for anode with high-capacity and ultralong-life lithium storage properties *Carbon* **115** 95–104
[7] Zhang H, Wang Y, Liu P, Chou S L, Wang J Z, Liu H, Wang G and Zhao H 2016 Highly ordered single crystalline nanowire array assembled three-dimensional $Nb_3O_7(OH)$ and Nb_2O_5 superstructures for energy storage and conversion applications *ACS Nano* **10** 507–14
[8] Song M Y, Kim N R, Yoon H J, Cho S Y, Jin H J and Yun Y S 2017 Long-lasting Nb_2O_5-based nanocomposite materials for Li-ion storage *ACS Appl. Mater. Interfaces* **9** 2267–74
[9] Sun Y, Tang J, Zhang K, Yuan J, Li J, Zhu D M, Ozawa K and Qin L C 2017 Comparison of reduction products from graphite oxide and graphene oxide for anode applications in lithium-ion batteries and sodium-ion batteries *Nanoscale* **9** 2585–95
[10] Liu C, Liu X, Tan J, Wang Q, Wen H and Zhang C 2017 Nitrogen-doped graphene by all-solid-state ball-milling graphite with urea as a high-power lithium ion battery anode *J. Power Sources* **342** 157–64
[11] Pang Q, Zhao Y, Bian X, Ju Y, Wang X, Wei Y, Liu B, Du F, Wang C and Chen G 2017 Hybrid graphene@MoS_2@TiO_2 microspheres for use as a high performance negative electrode material for lithium ion batteries *J. Mater. Chem.* A **5** 3667–74
[12] Zhang Y, Ma Z, Liu D, Dou S, Ma J, Zhang M, Guo Z, Chen R and Wang S 2017 p-Type SnO thin layers on n-type SnS_2 nanosheets with enriched surface defects and embedded charge transfer for lithium ion batteries *J. Mater. Chem.* A **5** 512–8
[13] Mahmood N, Tang T and Hou Y 2016 Nanostructured anode materials for lithium ion batteries: progress, challenge and perspective *Adv. Energy Mater.* **6** 1600374
[14] Griffith K J, Forse A C, Griffin J M and Grey C P 2016 High-rate intercalation without nanostructuring in metastable Nb_2O_5 bronze phases *J. Am. Chem. Soc.* **138** 8888–99
[15] An S J, Li J, Daniel C, Mohanty D, Nagpure S and Wood D L 2016 The state of understanding of the lithium-ion-battery graphite solid electrolyte interphase (SEI) and its relationship to formation cycling *Carbon* **105** 52–76
[16] Zhang W, Sheng J Z, Zhang J, He T, Hu L, Wang R, Mai L Q and Mu S C 2016 Hierarchical three-dimensional MnO nanorods/carbon anodes for ultralong-life lithium-ion batteries *J. Mater. Chem.* A **4** 16936–45
[17] Zhang W, Li J N, Zhang J, Sheng J Z, He T, Tian M Y, Zhao Y F, Xie C J, Mai L Q and Mu S C 2017 Top-down strategy to synthesize mesoporous dual carbon armored MnO nanoparticles for lithium-ion battery anodes *ACS Appl. Mater. Interfaces* **9** 12680–6
[18] Yan L, Rui X, Chen G, Xu W, Zou G and Luo H 2016 Recent advances in nanostructured Nb-based oxides for electrochemical energy storage *Nanoscale* **8** 8443–65
[19] Zhang C, Kim S J, Ghidiu M, Zhao M-Q, Barsoum M W, Nicolosi V and Gogotsi Y 2016 Layered orthorhombic Nb_2O_5@$Nb_4C_3T_x$and TiO_2@$Ti_3C_2T_x$ hierarchical composites for high performance Li-ion batteries *Adv. Funct. Mater.* **26** 4143–51
[20] Reddy M V, Jose R, Viet A L, Ozoemena K I, Chowdari B V R and Ramakrishna S 2014 Studies on the lithium ion diffusion coefficients of electrospun Nb_2O_5 nanostructures using galvanostatic intermittent titration and electrochemical impedance spectroscopy *Electrochim. Acta* **128** 198–202
[21] Chen D, Wang J H, Chou T F, Zhao B, El-Sayed M A and Liu M 2017 Unraveling the nature of anomalously fast energy storage in T-Nb_2O_5 *J. Am. Chem. Soc.* **139** 7071–81
[22] Lubimtsev A A, Kent P R C, Sumpter B G and Ganesh P 2013 Understanding the origin of high-rate intercalation pseudocapacitance in Nb_2O_5 crystals *J. Mater. Chem.* A **1** 14951–6
[23] Jiang J, Nie P, Ding B, Wu W, Chang Z, Wu Y, Dou H and Zhang X 2016 Effect of graphene modified Cu current collector on the performance of $Li_4Ti_5O_{12}$ anode for lithium-ion batteries *ACS Appl. Mater. Interfaces* **8** 30926–32
[24] Chiu H-C, Lu X, Zhou J, Gu L, Reid J, Gauvin R, Zaghib K and Demopoulos G P 2017 Capacity fade mechanism of $Li_4Ti_5O_{12}$ nanosheet anode *Adv. Energy Mater.* **7** 1601825
[25] Li X, Wu G, Liu X, Li W and Li M 2017 Orderly integration of porous TiO_2 (B) nanosheets into bunchy hierarchical structure for high-rate and ultralong-lifespan lithium-ion batteries *Nano Energy* **31** 1–8
[26] Augustyn V, Come J, Lowe M A, Kim J W, Taberna P-L, Tolbert S H, Abruña H D, Simon P and Dunn B 2013 High-rate electrochemical energy storage through Li^+ intercalation pseudocapacitance *Nat. Mater.* **12** 518–22
[27] Kim J W, Augustyn V and Dunn B 2012 The effect of crystallinity on the rapid pseudocapacitive response of Nb_2O_5 *Adv. Energy Mater.* **2** 141–8
[28] Li S, Xu Q, Uchaker E, Cao X and Cao G 2016 Comparison of amorphous, pseudohexagonal and orthorhombic Nb_2O_5 for high-rate lithium ion insertion *CrystEngComm* **18** 2532–40
[29] Cheong J Y, Kim C, Jung J W, Yoon K R, Cho S H, Youn D Y, Jang H Y and Kim I D 2017 Formation of a surficial bifunctional nanolayer on Nb_2O_5 for ultrastable electrodes for lithium-ion battery *Small* **13** 1603610

[30] Lim E *et al* 2015 Facile synthesis of Nb_2O_5@carbon core–shell nanocrystals with controlled crystalline structure for high-power anodes in hybrid supercapacitors *ACS Nano* **9** 7497–505

[31] Kong L, Zhang C, Wang J, Qiao W, Ling L and Long D 2015 Free-standing T-Nb_2O_5/graphene composite papers with ultrahigh gravimetric/volumetric capacitance for Li-ion intercalation pseudocapacitor *ACS Nano* **9** 11200–8

[32] Tao Y, Wei Y, Liu Y, Wang J, Qiao W, Ling L and Long D 2016 Kinetically-enhanced polysulfide redox reactions by Nb_2O_5 nanocrystals for high-rate lithium-sulfur battery *Energy Environ. Sci.* **9** 3230–9

[33] Liu S, Zhou J, Cai Z, Fang G, Cai Y, Pan A and Liang S 2016 Nb_2O_5 quantum dots embedded in MOF derived nitrogen-doped porous carbon for advanced hybrid supercapacitor applications *J. Mater. Chem.* A **4** 17838–47

[34] Wang J, Li H, Shen L, Dong S and Zhang X 2016 Nb_2O_5 nanoparticles encapsulated in ordered mesoporous carbon matrix as advanced anode materials for Li ion capacitors *RSC Adv.* **6** 71338–44

[35] Song H, Fu J, Ding K, Huang C, Wu K, Zhang X, Gao B, Huo K, Peng X and Chu P K 2016 Flexible Nb_2O_5 nanowires/graphene film electrode for high-performance hybrid Li-ion supercapacitors *J. Power Sources* **328** 599–606

[36] Lim E *et al* 2016 High-performance sodium-ion hybrid supercapacitor based on Nb_2O_5@carbon core–shell nanoparticles and reduced graphene oxide nanocomposites *Adv. Funct. Mater.* **26** 3711–9

[37] Arunkumar P, Ashish A G, Babu B, Sarang S, Suresh A, Sharma C H, Thalakulam M and Shaijumon M M 2015 Nb_2O_5/graphene nanocomposites for electrochemical energy storage *RSC Adv.* **5** 59997–60004

[38] Kim H, Lim E, Jo C, Yoon G, Hwang J, Jeong S, Lee J and Kang K 2015 Ordered-mesoporous Nb_2O_5/carbon composite as a sodium insertion material *Nano Energy* **16** 62–70

[39] Wang X, Li G, Tjandra R, Fan X, Xiao X and Yu A 2015 Fast lithium-ion storage of Nb_2O_5 nanocrystals *in situ* grown on carbon nanotubes for high-performance asymmetric supercapacitors *RSC Adv.* **5** 41179–85

[40] Kong L, Zhang C, Wang J, Qiao W, Ling L and Long D 2016 Nanoarchitectured Nb_2O_5 hollow, Nb_2O_5@carbon and NbO_2@carbon core–shell microspheres for ultrahigh-rate intercalation pseudocapacitors *Sci. Rep.* **6** 21177

[41] Xing L L, Huang K J and Fang L X 2016 Preparation of layered graphene and tungsten oxide hybrids for enhanced performance supercapacitors *Dalton Trans.* **45** 17439–46

[42] Xing L L, Zhao G G, Huang K J and Wu X 2018 A yolk-shell V_2O_5 structure assembled from ultrathin nanosheets and coralline-shaped carbon as advanced electrodes for a high-performance asymmetric supercapacitor *Dalton Trans.* **47** 2256–65

[43] Xing L L, Huang K J, Cao S X and Pang H 2018 Chestnut shell-like $Li_4Ti_5O_{12}$ hollow spheres for high-performance aqueous asymmetric supercapacitors *Chem. Eng. J.* **332** 253–9

[44] Wang X, Yan C, Yan J, Sumboja A and Lee P S 2015 Orthorhombic niobium oxide nanowires for next generation hybrid supercapacitor device *Nano Energy* **11** 765–72

[45] Kong L, Zhang C, Zhang S, Wang J, Cai R, Lv C, Qiao W, Ling L and Long D 2014 High-power and high-energy asymmetric supercapacitors based on Li^+-intercalation into a T-Nb_2O_5/graphene pseudocapacitive electrode *J. Mater. Chem.* A **2** 17962–70

[46] Lim E *et al* 2014 Advanced hybrid supercapacitor based on a mesoporous niobium pentoxide/carbon as high-performance anode *ACS Nano* **8** 8968–78

[47] Lee B-G and Lee S-H 2017 Application of hybrid supercapacitor using granule $Li_4Ti_5O_{12}$/activated carbon with variation of current density *J. Power Sources* **343** 545–9

[48] Guo W, Li Y, Tang Y, Chen S, Liu Z, Wang L, Zhao Y and Gao F 2017 TiO_2 nanowire arrays on titanium substrate as a novel binder-free negative electrode for asymmetric supercapacitor *Electrochim. Acta* **229** 197–207

[49] Wang X and Shen G 2015 Intercalation pseudo-capacitive $TiNb_2O_7$@carbon electrode for high-performance lithium ion hybrid electrochemical supercapacitors with ultrahigh energy density *Nano Energy* **15** 104–15

[50] Wang X, Li G, Chen Z, Augustyn V, Ma X, Wang G, Dunn B and Lu Y 2011 High-performance supercapacitors based on nanocomposites of Nb_2O_5 nanocrystals and carbon nanotubes *Adv. Energy Mater.* **1** 1089–93

[51] Kong L, Cao X, Wang J, Qiao W, Ling L and Long D 2016 Revisiting Li^+ intercalation into various crystalline phases of Nb_2O_5 anchored on graphene sheets as pseudocapacitive electrodes *J. Power Sources* **309** 42–9

[52] Lübke M, Sumboja A, Johnson I D, Brett D J L, Shearing P R, Liu Z and Darr J A 2016 High power nano-Nb_2O_5 negative electrodes for lithium-ion batteries *Electrochim. Acta* **192** 363–9

[53] Liu S, Zhou J, Cai Z, Fang G, Pan A and Liang S 2016 Nb_2O_5 microstructures: a high-performance anode for lithium ion batteries *Nanotechnology* **27** 46LT01

[54] Liu M, Yan C and Zhang Y 2015 Fabrication of Nb_2O_5 nanosheets for high-rate lithium ion storage applications *Sci. Rep.* **5** 8326

[55] Cheong J Y, Jung J-W, Youn D-Y, Kim C, Yu S, Cho S-H, Yoon K R and Kim I-D 2017 Mesoporous orthorhombic Nb_2O_5 nanofibers as pseudocapacitive electrodes with ultra-stable Li storage characteristics *J. Power Sources* **360** 434–42

[56] Senthil C, Kesavan T, Bhaumik A, Yoshio M and Sasidharan M 2017 Nitrogen rich carbon coated TiO_2 nanoparticles as anode for high performance lithium-ion battery *Electrochim. Acta* **255** 417–27

[57] Zhu K, Gao H, Hu G, Liu M and Wang H 2017 Scalable synthesis of hierarchical hollow $Li_4Ti_5O_{12}$ microspheres assembled by zigzag-like nanosheets for high rate lithium-ion batteries *J. Power Sources* **340** 263–72

[58] Lou S *et al* 2017 Superior performance of ordered macroporous $TiNb_2O_7$ anodes for lithium ion batteries: understanding from the structural and pseudocapacitive insights on achieving high rate capability *Nano Energy* **34** 15–25